

# A Simple $\text{Cl}^-$ -Free Electrolyte Based on Magnesium Nitrate for Magnesium–Sulfur Battery Applications

Eslam Sheha,\* Mohamed Farrag, Shengqi Fan, Eman Kamar, and Niya Sa\*

Cite This: *ACS Appl. Energy Mater.* 2022, 5, 2260–2269

Read Online

ACCESS |



Metrics &amp; More



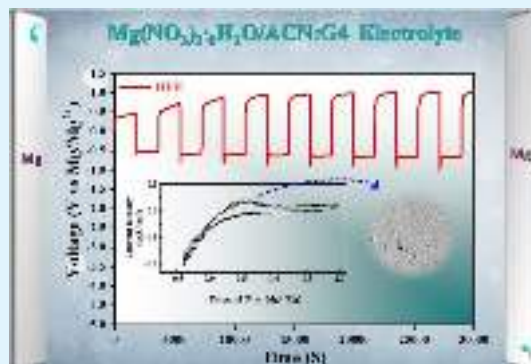
Article Recommendations



Supporting Information

**ABSTRACT:** The magnesium–sulfur (MgS) battery is a promising alternative to the post-lithium battery because of its low-cost construction, eco-friendliness, high theoretical energy density, and safety. However, the lack of simple compatible electrolytes, self-discharge, polysulfide shuttle effect, and the slow conversion reaction pathway still limit its practical applications. Here, we propose a simple halogen-free electrolyte (HFE) based on  $\text{Mg}(\text{NO}_3)_2$  dissolved in the cosolvent of acetonitrile (ACN) and tetraethylene glycol dimethyl (G4) that applies to a Mg/S full cell. The as-prepared Mg-ion electrolyte exhibits efficient Mg plating/stripping performance, high anodic stability (vs  $\text{Mg}/\text{Mg}^{2+}$ ), and a high ionic conductivity of  $\sim 10^{-4} \text{ S cm}^{-1}$  at 313 K. Chronoamperometry (CA), scanning electron microscopy, and energy-dispersive spectroscopy examinations report that the HFE supports flat, dendrite-free, and translucent Mg deposits. Polymer layer interface (PLI)-based polyvinylidene fluoride (PVDF) and  $\text{Mg}(\text{O}_3\text{SCF}_3)_2$  have been designed to isolate the surface of the Mg anode from the liquid electrolyte. A sulfur cathode with the anchoring materials of silicon carbide and barium titanate-based material has been designed and characterized. The Mg/S battery has been constructed with an initial discharge capacity of up to  $1200 \text{ mAh g}^{-1}$ , and it has retained a reversible capacity at  $100 \text{ mAh g}^{-1}$  after 10 cycles. This study offers a pivotal role in designing a promising HFE candidate for a high-performance MgS battery.

**KEYWORDS:** magnesium-ion battery, halogen-free electrolyte, sulfur, polymer interface, polysulfide



## INTRODUCTION

Rechargeable Mg–S batteries are among the best candidates for mitigating climate change and bridging the gap of renewable energy intermittency these days because of their low-cost construction, eco-friendliness, high theoretical energy density, and safety. The characteristics of the magnesium–sulfur battery are twofold. The first is that a Mg anode exhibits resistance to dendrite growth at low current density, higher volumetric capacity, abundance in the Earth's crust, and low cost.<sup>1</sup> The second is that a sulfur (S) cathode offers low cost ( $\$150 \text{ ton}^{-1}$ ),<sup>2</sup> high theoretical capacity of  $1673 \text{ mAh g}^{-1}$ , and nontoxicity. Hence, integrating a Mg anode, a sulfur cathode, and an efficient electrolyte in a full cell yields a theoretical specific energy of  $3200 \text{ Wh L}^{-1}$ <sup>3–6</sup> and a thermodynamic voltage of 1.77 V. The shuttle of polysulfide, inactive materials, excessive demand of electrolytes, limited compatible electrolyte with electrophilic sulfur, and sluggish kinetic conversion reaction for Mg-ion storage are essential challenges to realize practical technology.<sup>7</sup> In this regard, recent innovative strategies have been devoted toward developing non-nucleophilic electrolytes to be compatible with the electrophilic nature of sulfur; for example,  $\text{Mg}(\text{CF}_3\text{SO}_3)_2\text{--AlCl}_3$  dissolved in a cosolvent of tetrahydrofuran and tetraglyme,<sup>8</sup>  $\text{Mg}(\text{CF}_3\text{SO}_3)_2$ ,  $\text{MgCl}_2$ , and  $\text{AlCl}_3$  in 1,2-dimethoxyethane

(DME),<sup>9–11</sup> organic magnesium borate-based electrolyte,<sup>12</sup> and halogen-free electrolyte (HFE) like  $\text{Mg}[\text{B}(\text{hfp})_4]_2$ .<sup>13,14</sup> However, shortcomings and unsolved problems such as poor chemical stability, the corrosion nature of Cl on battery components, the cost and complex synthesis constitution of  $\text{Mg}[\text{B}(\text{hfp})_4]_2$ , and self-discharge restrict the commercialization of the electrolyte.<sup>15–18</sup>

On the other hand, attempts have been made for designing appropriate sulfur hosts to balance volume expansion upon magnesiation of sulfur, promote capacity and cycling performances, reduce polysulfide-shuttling, and improve the redox kinetics, hence improving the battery performance. For example, anchoring S in the structure of metal–organic derivative carbon, Se-doped sulfur–carbon composite, and  $\text{Co}_3\text{S}_4\text{@MXene}$  heterostructure promotes electrochemical kinetics via trapping soluble polysulfides.<sup>1,2,19</sup> The multifunctional additive of piezoelectric materials like  $\text{BaTiO}_3$  enabled

Received: December 1, 2021

Accepted: January 21, 2022

Published: February 2, 2022



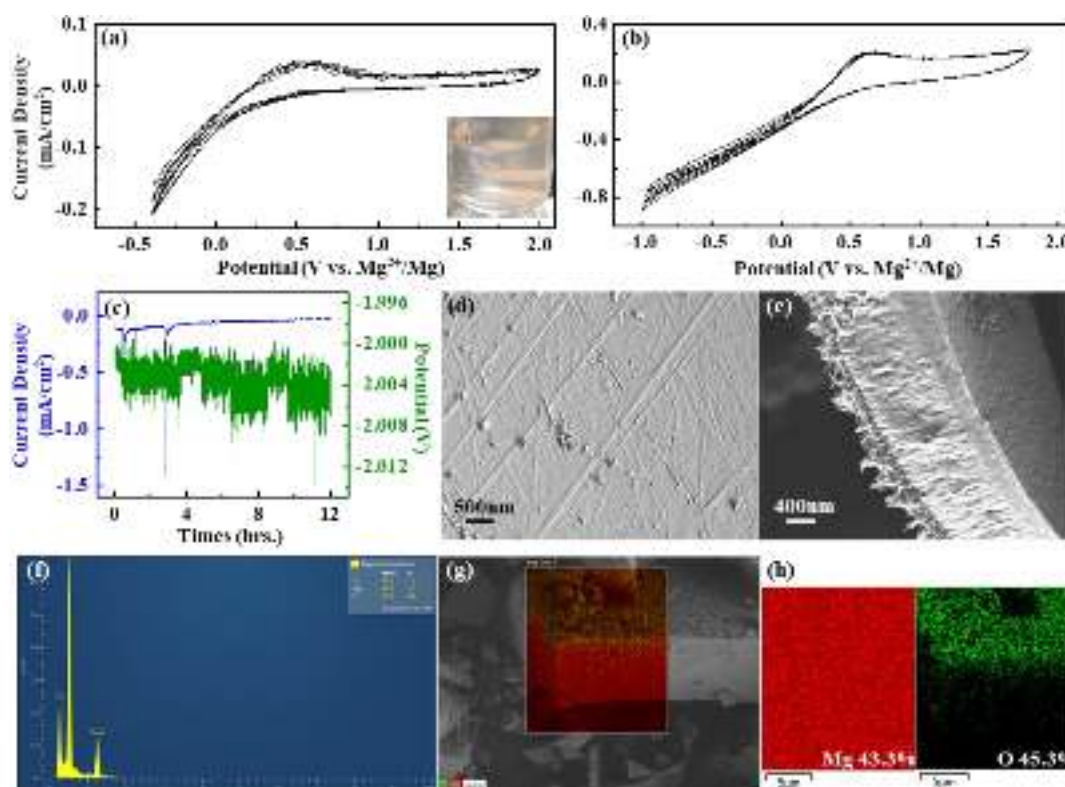


**Figure 1.** CVs in HFE (0.69 M  $\text{Mg}(\text{NO}_3)_2 \cdot 6\text{H}_2\text{O}$  in ACN:G4 (~2:1) on the Pt working electrode at a scan rate of  $50 \text{ mV s}^{-1}$ ; (a) at room temperature, (b) at  $55^\circ\text{C}$ ; (c) chronoamperometry current responses on Mg upon contact with the HFE electrolyte after 12 h of plating at room temperature; (d, e) SEM images of electrochemically plated Mg metal; (f–h) EDS and elemental mapping images for electrochemically plated Mg in the HFE electrolyte.

high migration of Li ions during the discharging process via converting the effect of electrochemical stress into the electrostatic force, such that charges on the surface of ferroelectrics can guarantee polar polysulfide molecules the continuity of electrochemical reaction.<sup>20–23</sup> Furthermore, SiC and  $\text{B}_4\text{C}$  are other stable and effective anchoring materials to restrain the shuttle of soluble lithium polysulfide due to the polar groups and chemical stabilities of carbide.<sup>24–26</sup> According to the above concerns, this study is an attempt to address some of the MgS issues via novel and mimic approaches; the first approach includes, for the first time, developing a simple HFE via simple mixing of commercially available non-nucleophilic  $\text{Mg}(\text{NO}_3)_2$  in cosolvent of ACN and G4. The second approach considers integrating sulfur with graphene nanoplatelets (GNPs) and different stoichiometric ratios of  $\text{BaTiO}_3/\text{SiC}$  via the sonochemical method aiming at restraining the shuttle movement of polysulfide and bypassing the sluggish kinetics. The third approach is designing PLI-based polyvinylidene fluoride (PVDF) and  $\text{Mg}(\text{O}_3\text{SCF}_3)_2$  to isolate the surface of the Mg anode from the liquid electrolyte. The prepared electrolytes were investigated by electrochemical impedance spectroscopy (EIS), overpotentials of Mg dep./diss., cyclic voltammetry (CV), and linear sweep voltammetry (LSV). To investigate the practical use of the developed electrolytes and cathodes, full MgS cells have been fabricated, and electrochemical performances have been evaluated. The highest initial capacity of  $\sim 1200 \text{ mAh g}^{-1}$  at  $200 \text{ mA g}^{-1}$  is obtained for the optimized cells. Furthermore, X-ray diffraction (XRD), energy-dispersive X-ray spectroscopy (EDS), and scanning electron microscopy (SEM) are carried out to

elucidate the reversible magnesium-storage mechanism at different cycling states.

## EXPERIMENTAL TECHNIQUES

**Electrolyte Synthesis.** Magnesium nitrate  $\text{Mg}(\text{NO}_3)_2 \cdot 6\text{H}_2\text{O}$  (Alfa Aesar 98%) salt was preheated at  $80^\circ\text{C}$  to remove the moisture molecules. Preheated  $\text{Mg}(\text{NO}_3)_2 \cdot 6\text{H}_2\text{O}$  (1.5 g) was dissolved in 5.4:2.7 mL of ACN/G4 to obtain HFE. PLI was synthesized by dissolving 1 g of PVDF in 20 mL of methyl-2-pyrrolidinone (NMP) and stirred for 24 h; then, 0.45 g of  $\text{Mg}(\text{O}_3\text{SCF}_3)_2$  and 6 wt. % nanoparticles silica fume were added to the solution and stirred for 24 h. The resulting slurry was coated on a glass sheet using a mini coater (MC-20, Hohsen) and dried in a normal environment. The resulting film was then cut to a 19.4 mm disc diameter and dried at 328 K in a vacuum oven.

**Cathode Synthesis.** Sulfur (S, Alfa Aesar 99%), silicon carbide (SiC, Qualicum 99%), BTO (Alfa Aesar 99%), and GNPs (Grade M, XG Science) composite have been synthesized via the sonochemical technique. First, 0.5 g of  $50\text{wt \% S}_{(40-x)}\text{wt \% SiC}_{x}\text{wt \% BTO}_{10}\text{wt \% GNP}$  ( $x = 0, 10$ , and  $20$ ) was ground and dispersed using an ultrasonicator (1000 watt) in  $100 \text{ cm}^3$  deionized water via high power to thoroughly exfoliate the graphene sheets. The resulting mixture was dried in an oven at  $100^\circ\text{C}$  for 24 h to obtain three samples denoted as follows:  $\text{S}_1$  ( $x = 0$ ),  $\text{S}_2$  ( $x = 10$ ), and  $\text{S}_3$  ( $x = 20$ ). After that, the three samples were initially heat-treated at  $200^\circ\text{C}$  for 2 h to infiltrate the melted elemental sulfur into the graphene layer. Then, the temperature was further increased and fixed at  $300^\circ\text{C}$  for 2 h to coat vaporized sulfur onto graphene and obtain another three samples denoted as follows:  $\text{H-S}_1$ ,  $\text{H-S}_2$ , and  $\text{H-S}_3$ .

**Material Characterization.** XRD patterns were obtained through a PANalytical XRD equipment model X'Pert PRO (Cu-radiation,  $\lambda = 1.542 \text{ \AA}$ ). The morphology was investigated using a field emission scanning electron microscope (FE-SEM, Quanta 250 FEG) with an

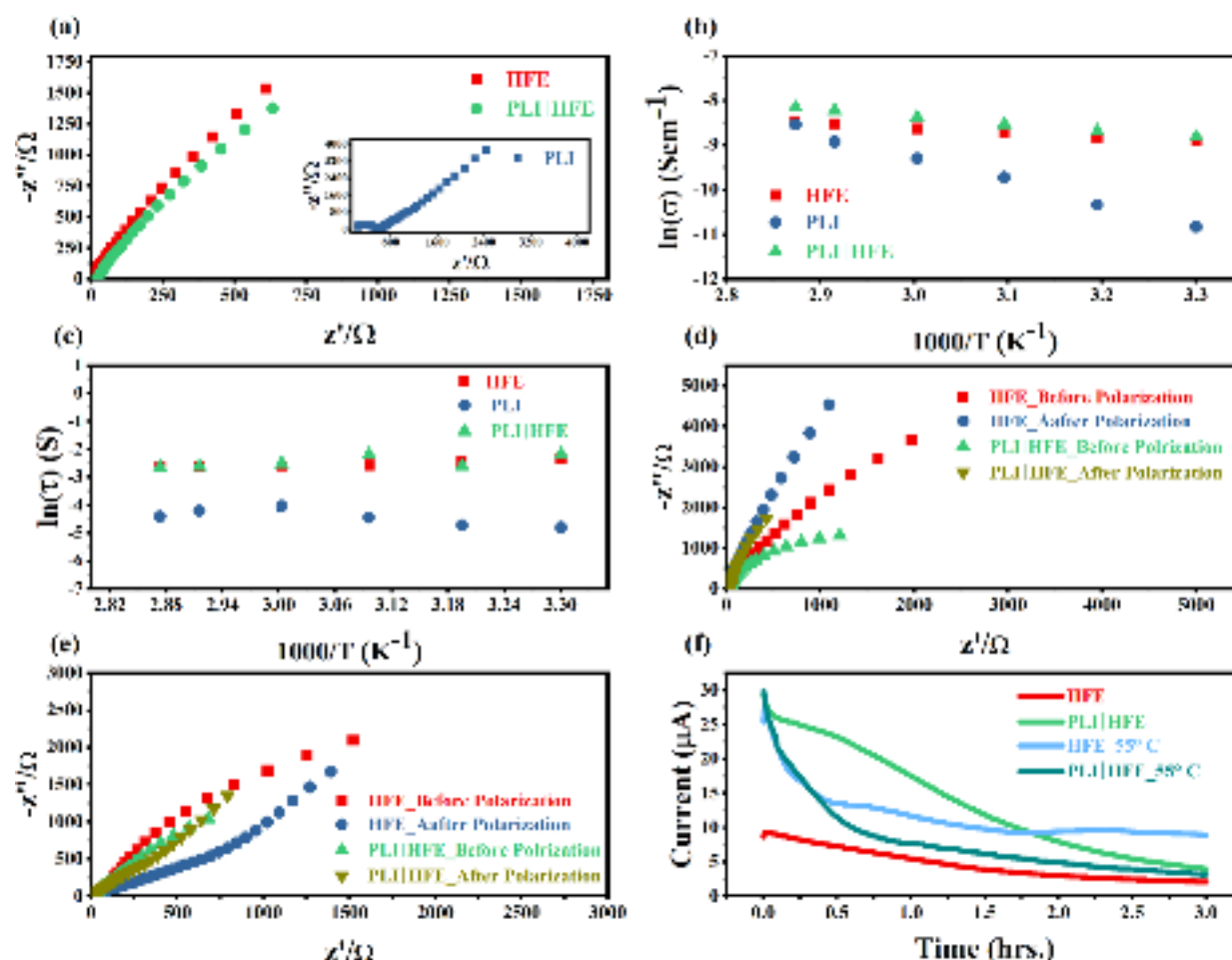


**Figure 2.** (a) Nyquist plots of a symmetric SS|electrolyte|SS cell at 50 °C; (b) Arrhenius plot; (c) relaxation time vs reciprocal of temperature; Nyquist plots of symmetric Mg|electrolyte|Mg cells before and after polarization (d) at room temperature and (e) at 55 °C; (f) polarization current curve vs time of symmetric Mg|electrolyte|Mg cells.

attached energy-dispersive X-ray (EDS) unit. The structure of the cathode at different cycling states was characterized via a Rigaku MiniFlex 600 diffractometer.

**Electrochemical Measurements.** Cyclic voltammograms were characterized in an electrochemical cell assembled with Mg foil as the reference electrode and the counter electrode and Pt disk as the working electrode. Ionic conductivity ( $\sigma$ ) of all electrolyte samples was measured between 1 MHz and 10 Hz at different temperatures using the CHI604E electrochemical workstation in a SS|electrolyte|SS electrolytic cell;  $\sigma = \frac{t}{R \times A}$ , where  $R$  is the resistance,  $A$  is the effective overlap area of SS foils, and  $t$  is the distance between two SS foils. The electrochemical stability of the electrolyte was measured using a two-electrode coin cell with stainless steel as a working electrode and Mg foil as both the reference and counter electrodes. The electrochemical performance of the MgS battery was conducted using a coin-type cell (CR2032), which was assembled in an argon environment. The working electrode was prepared by mixing 75:15:10 wt. % of  $S_n$  or  $H_{-}S_m$  ( $n = 1, 2$ , and 3) PVDF binder and carbon Super-P in an NMP solvent with stirring thoroughly to obtain homogeneous slurry. The slurry was pasted on a pure Al sheet using a mini coater (MC-20, Hohsen) and dried in an oven at 100 °C for 2 h; the loading density of the active material ( $S$ ) is about 1 mg/cm<sup>2</sup>. Glass fiber was used as the separator. The discharge/charge tests were conducted between 0.1 and 2.5 V cutoff voltages (vs  $Mg^{2+}/Mg$ ) using a NEWARE BTS4000 tester. Magnesiumation and demagnesiumation of  $S_n$  and  $H_{-}S_m$  were performed by initial discharge/charge of the coin cells. Before XRD, SEM, and EDS analyses, the cells were disassembled, and the

collected cathode disks were washed by rinsing twice in ACN and drying at 60 °C for 30 min.

## RESULTS AND DISCUSSION

Adding G4 as a cosolvent to  $Mg(NO_3)_2 \cdot 6H_2O$  in ACN results in a translucent solution (Figure 1a, inset), which invites the evaluation of the capability of this electrolyte for Mg stripping/plating. Figure 1a, b shows cyclic voltammograms for Mg plating/stripping on a Pt electrode from solutions of HFE (0.69 M  $Mg(NO_3)_2 \cdot 6H_2O$  in ACN:G4 (~2:1)) at room temperature and at 55 °C, respectively. The results indicate that the HFE solutions allow reversible Mg deposition/dissolution, and the potential window increases with the increase in the temperature to 55 °C, which reflects the increase in the ionic conductivity due to ion dissociation with an increase in the temperature. Figure S1a and b shows the relation between the plating/stripping current and the elapsed time at room temperature and at 55 °C, respectively. The Coulombic efficiency (CE) of Mg plating/stripping is calculated by integrating the area of plating/stripping segments. The average CE values are listed in Table S1, and it can be noticed that the value of CE ca. 32.69% at RT is higher than the value of CE ca. 23.53% at 55 °C. The reduction in the value of CE with increasing temperature can be speculated as the temperature plays a contradictory role; the first enhances the ionic mobility of  $Mg^{2+}$ , while the second increases the



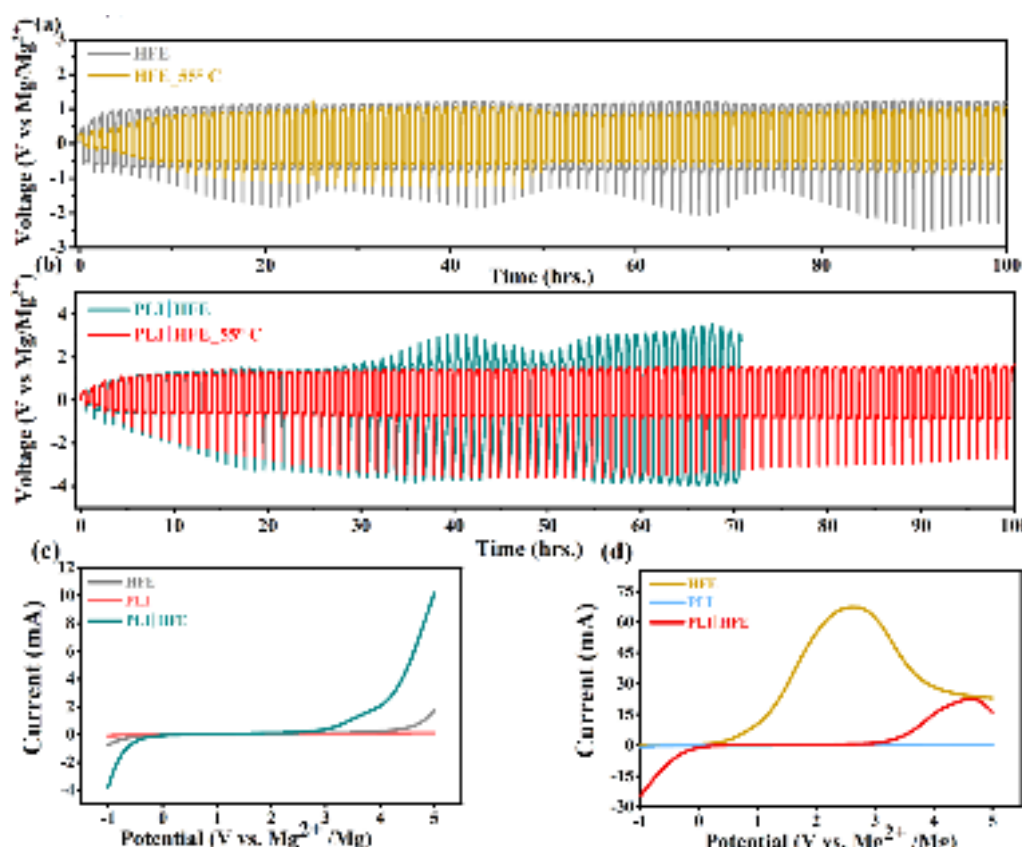


**Figure 3.** Stripping/plating of Mg//electrolytes//Mg cells (a) HFE and (b) PLI|HFE electrolytes; (c, d) LSV of Mg//electrolytes//SS cells at room temperature and at 55 °C, respectively.

kinetics of parasitic reactions that suppress the Mg plating/stripping rate.<sup>27</sup> The chronoamperometry (CA) profile is shown in Figure 1c, the plating time is 12 h, and the samples collected on the electrode surface are nondendritic, flat, and translucent crystals of the Mg element, as verified by the SEM image and EDS results in Figure 1d–e and Figure 1f, respectively. Figure 1g, h shows the elemental mapping images of the post-run working electrodes of the CA studies in the HFE electrolyte. It is clear to see the homogeneous distribution and higher concentration (up to 43.4 wt %) of the Mg element. Figure 2a illustrates the Nyquist plots of a symmetrical SS|HFE|SS or SS|PLI|HFE|SS coin cell with the inset showing the Nyquist plots of SS|PLI|SS. The HFE and PLI|HFE show an incomplete semicircle at higher frequencies and a spike at low frequencies. The diameter of the semicircle, which represents the bulk resistance ( $R_b$ ), shrinks with increasing temperature. Mg-ion conduction in HFE, PLI, and PLI|HFE electrolytes shows a thermally activated process according to the Arrhenius equation  $\sigma = \sigma_0 \exp^{-E_a/KT}$ , where  $\sigma_0$  represents the pre-exponential factor of conductivity, and  $K$  is the Boltzmann constant. Figure 2b shows the fitting curves of logarithmic conductivity against the inverse of the temperature of the HFE, PLI|HFE, and PLI electrolytes. From the linear fit curve slope, the calculated activation energies are 0.1, 0.45, and 0.13 eV, respectively, indicating a lower energy barrier for  $Mg^{2+}$  migration in the liquid and the dual electrolyte.<sup>28</sup> The relaxation time is estimated from the relation  $-\frac{v}{u} = (\omega\tau)^{1-h}$ , where  $v$ ,  $u$ , and  $h = 2\alpha/\pi$  are the distance between an experimental point and ( $O$ ,  $R_b$ ), the distance between the experimental point and (0, 0), and the

depressed angle from the  $Z'$ -axis, respectively, and  $\omega$  is the angular frequency. Relaxation time for the HFE, PLI, and PLI|HFE electrolytes decreases with the increase in temperature, while for PLI, the value initially increases up to 60 °C and then decreases (Figure 2c). Generally, the change in the value of  $\tau$  depends on the change in the viscosity of the medium that affects the freedom of the dipoles. The  $Mg^{2+}$  transference number value  $t_{Mg}^{2+}$  is an essential parameter that controls the kinetics of Mg stripping/plating. EIS was conducted before and after DC polarization ( $V = 0.1$  V) to derive the initial  $R_0$  and steady-state  $R_s$  charge-transfer resistances. The  $Mg^{2+}$  ion transference number was calculated according to the following

Bruce Vincent eq.  $t_{Mg^{2+}} = \left[ \frac{I_s(\Delta V - R_0 I_0)}{I_0(\Delta V - R_s I_s)} \right]$ , where  $I_0$ ,  $I_s$  and  $R_0$ ,  $R_s$

refer to the initial current and the steady-state current, respectively, Figure 2d, e and S2a. The polarization current versus time was recorded and is shown in Figure 2f and S2b. The values of  $t_{Mg}^{2+}$  are 0.83, 0.78, and 0.97 at room temperature and 0.87, 0.69, and 0.93 at 55 °C, for HFE, PLI, and PLI|HFE, respectively. Figure 3a, b shows Mg stripping/plating curves of the symmetric Mg|Mg cells containing HFE and PLI|HFE electrolytes, respectively. The cells exhibit good cycling stability at ambient temperature (55 °C) with a minimal overpotential of <1 V at a current density of 20  $\mu A cm^{-2}$  for more than 100 h than the symmetric Mg|Mg cells at room temperature. This behavior reflects the efficient transport properties of the electrolyte.<sup>29</sup> Figure 3c,d shows LSV scans of the HFE, PLI, and PLI|HFE electrolytes run on an asymmetrical cell of the SS|electrolyte|Mg cell at room temperature and 55 °C. HFE, PLI, and PLI|HFE remain stable at up to 3.8, 4, >5 V vs  $Mg^{2+}/Mg$ , respectively, at room temperature. At 55

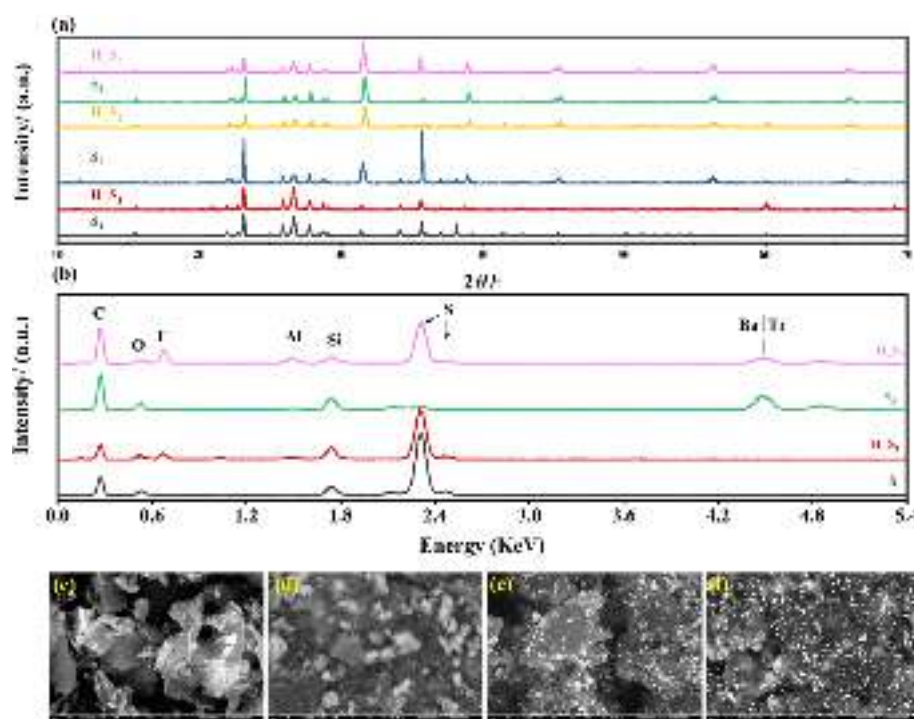


**Figure 4.** (a) XRD patterns; (b) EDS spectra of the sulfur cathodes at different synthetic states; SEM micrographs of (c)  $S_1$ , (d)  $H_{S1}$ , (e)  $S_3$ , and (f)  $H_{S3}$ .

°C, HFE and PLIHFEE displayed broad peaks at about 2.63 and 4.6 V, respectively, which is probably due to the electrolyte decomposition.<sup>30</sup> The shift of the peak position to high voltage after the introduction of the PLI reflects its role in optimizing the oxidation stability of the electrolyte at different temperatures. The XRD pattern of  $S_n$  and  $H_{S_n}$  composites (Figure 4a) reveals peaks at  $2\theta = 15.47^\circ, 23.16^\circ, 25.89^\circ, 27.81^\circ$ , and  $28.74^\circ$  that correspond to (113), (222), (026), (206), and (313) lattice planes of the sulfur orthorhombic structure with space group:  $Fddd$  (70), and  $a = 10.437 \text{ \AA}$ ,  $b = 12.845 \text{ \AA}$ , and  $c = 24.369 \text{ \AA}$ , which is in good agreement with the reported results [(JCPDS) card No. 74-1465].<sup>31</sup> It can be noticed that, after the heat treatment, the intensity of characteristic sulfur peaks for  $H_{S_n}$  is reduced compared with that for  $S_n$  samples, indicating mass loss that occurs mainly in the 150–300 °C range because of the partial sublimation of sulfur. The introduction of SiC within the framework of orthorhombic sulfur reveals four sharp peaks at about  $2\theta = 35.74^\circ, 41.47^\circ, 60.03^\circ$ , and  $71.68^\circ$  corresponding to (006), (101), (110), and (116) crystal planes of a hexagonal phase SiC with space group:  $P63mc$  (186);  $a = 3.081 \text{ \AA}$ ,  $b = 3.081 \text{ \AA}$ ,  $c = 15.124 \text{ \AA}$  [(JCPDS) card no. 75-831]. The characteristic peak of the GNP (002) reflection plane was observed at  $2\theta = 26.79^\circ$ <sup>32,33</sup> and matches well with the JCPDS card no. 08-0415, which confirms the hexagonal crystal structure with the  $P63/mmc$  space group. The introduction of BTO within the framework of  $S_{-}SiC$  results in new reflection planes located at  $2\theta = 22.42^\circ, 31.69^\circ, 45.53^\circ$ , and  $56.40^\circ$  that are assigned to the crystal planes of (100), (101), (200), and (211), which matches well with the reported data (JCPDS card No. 01-083-1875).<sup>34</sup> The lattice parameters of tetragonal BTO are observed to be  $a = b = 3.991 \text{ \AA}$ ,  $c = 4.025 \text{ \AA}$ , and  $\alpha = \beta = \gamma = 90^\circ$ , with space group  $P4mm$  (99). All major peaks of S, SiC, and BTO are well indexed without any impurity phase appearing, assuring the purity of the synthesized composites.

Figure 4b displays the EDS spectrum of  $S_n$  composites. The spectrum shows characteristic bands indexed to S, Si, Ba, Ti, O, and C elements and coincides with the balance of the starting materials. Figure 4c, d, e, f presents the SEM images of  $S_1$ ,  $H_{S1}$ ,  $S_3$ , and  $H_{S3}$  composites, respectively. As shown in Figure 4d, an exfoliated sample with sulfur and SiC decorated the curled GNP nanoplatelets. After the heat treatment of  $S_1$ , the evaporated elemental S was seeded as islands at the surface of the microflakes. The introduction of BTO particles results in a homogeneous distribution of well-defined microspheres of  $BaTiO_3$  with sizes of 1–2  $\mu\text{m}$  at the surface of microflakes, regardless of whether before ( $S_3$ ) and after the heat treatment ( $H_{S3}$ ); it is noteworthy that BTO looks like traps that can significantly suppress the shuttle effect.<sup>35</sup> Figure 5a, b shows CV curves between 0.3 and 2.5 V at a 20 mV/s scan rate of  $Mg|HFE|S_{1,2}$  and  $Mg|PLIHFEE|S_{1,2}$  cells for the initial five cycles at 55 °C, respectively. A prominent cathodic peak was observed at 0.15–0.35 V corresponding to sulfur conversion to long- and short-chain polysulfides via the  $S_{-}BTO_{-}SiC$  skeleton.<sup>36</sup> Furthermore, the anodic peak at  $\sim 2.16 \text{ V}$  can be attributed to the reoxidation of the discharge products, and CV curves of  $S_2$  have a more significant current density than that of  $S_1$ . They are owing to the introduction of BTO, which enabled the high migration of  $Mg^{2+}$  during the redox process via converting the effect of electrochemical stress into the electrostatic force and holding polar polysulfide molecules that allow for the active material to continue the electrochemical reaction. Broad anodic peaks (at  $\sim 2.2 \text{ V}$ ) corresponding to discharge product reoxidation were observed for  $S_1$  and  $S_2$ . In the subsequent cathodic and anodic scans, the intensity of the redox peaks was reduced to lower values because of the growth of the nonconductive  $Mg^{2+}$  passive layer at the Mg/electrolyte interface that should arise from the chemical decomposition of electrolyte components. The magnesium diffusion coefficient ( $D_{Mg}^{2+}$ ) is the key parameter

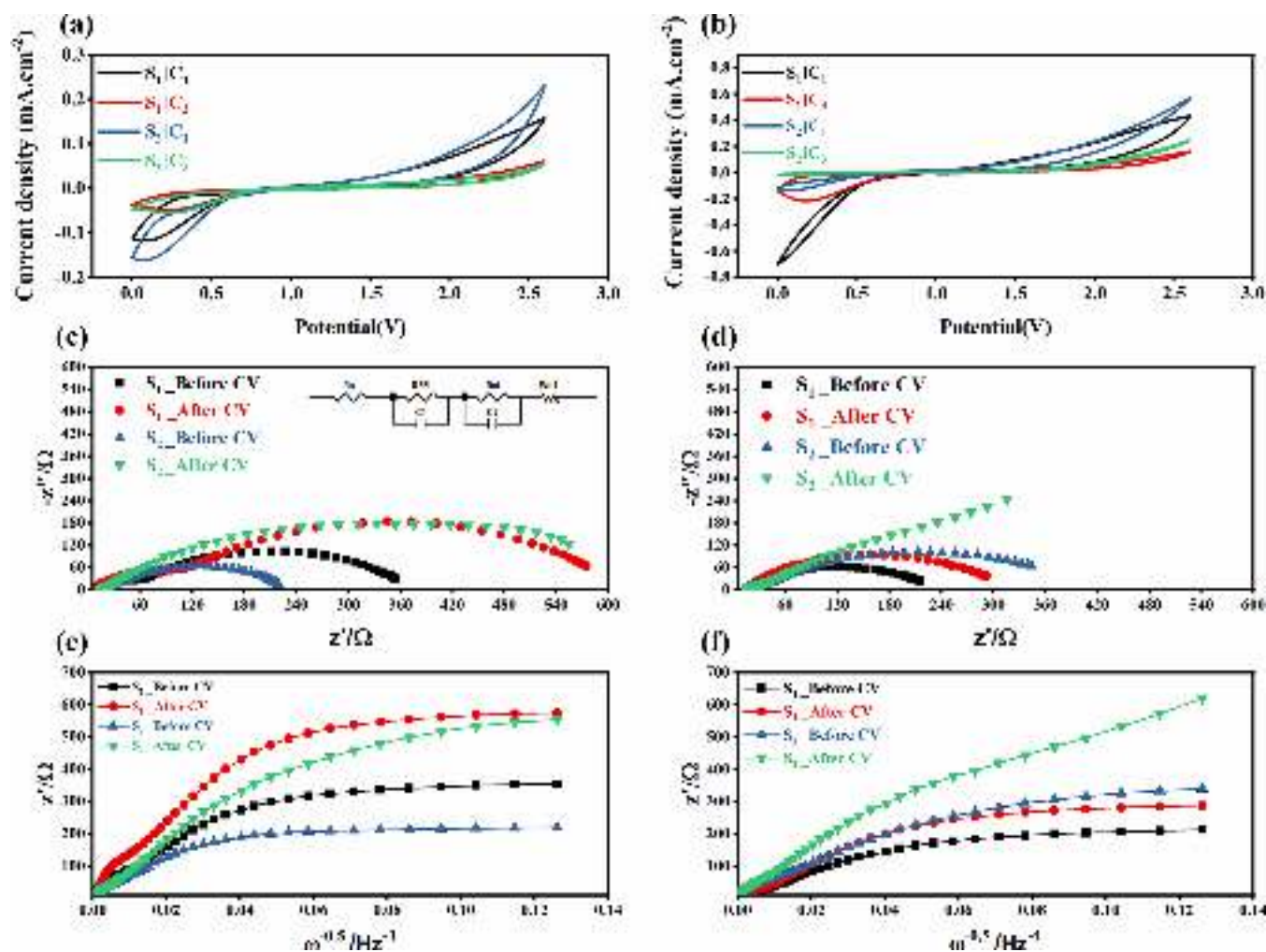


**Figure 5.** CV curve of the samples [ $S_1$ ,  $S_2$ ] at a scan rate of  $20 \text{ mV s}^{-1}$  (a) HFE, (b) PLI/HFE; EIS, (c) HFE, (d) PLI/HFE; linear fitting of Warburg impedance (e) HFE, (f) PLI/HFE; at  $55^\circ\text{C}$ .

**Table 1.** Comparison of the Evaluated Electrochemical Impedance Parameters of S Electrodes

EIS parameters	$R_s$ ( $\Omega$ )	$R_{SEI}$ ( $\Omega$ )	$R_{ct}$ ( $\Omega$ )	C1 (F)	C2 (F)	$A_w$ ( $\Omega$ )	$D_{Mg}^{2+}$ [ $\text{cm}^2 \text{s}^{-1}$ ]
HFE/ $S_1$	10.53	37.77	195.5	$1.3 \times 10^{-7}$	$5.96 \times 10^{-6}$	278	$1.02 \times 10^{-14}$
HFE/ $S_2$	13.49	6.695	33.74	$6.92 \times 10^{-7}$	$3.3 \times 10^{-6}$	129	$4.37 \times 10^{-14}$
PLI/HFE/ $S_1$	15.98	25.33	64.93	$5.38 \times 10^{-6}$	$7.56 \times 10^{-6}$	305	$8.44 \times 10^{-15}$
PLI/HFE/ $S_2$	13.06	6.775	124.2	$4.13 \times 10^{-7}$	$4.27 \times 10^{-5}$	748	$1.4 \times 10^{-15}$

that describes the transport of magnesium inside the cathode, that is, from the surface to the core and vice versa. Figure 5c,d illustrates the Nyquist plots of Mg/HFE/ $S_{1,2}$  and Mg/PLI/HFE/ $S_{1,2}$  coin cells before and after CV. The impedance response of the batteries was modeled using the equivalent circuit according to the ZView software, where  $R_s$ ,  $R_{SEI}$ , and  $R_{ct}$  are the Ohmic resistance of the bulk cell, the resistance of the interfacial layer, and the charge-transfer resistance, respectively. The low-frequency dispersion represents the Warburg impedance and is related to the diffusion of  $Mg^{2+}$  ( $D_{Mg}^{2+}$ ) in the electrode ( $W$ ). The fitted EIS parameters for  $S_1$  and  $S_2$  are presented in Table 1. The  $D_{Mg}^{2+}$  connect of  $S_1$  and  $S_2$  was measured by the Warburg region according to the equation<sup>37</sup>

$$D_{Mg}^{2+} = \frac{R^2 T^2}{2A^2 n^4 F^4 C^2 A_w^2},$$

and the Warburg coefficient ( $A_w$ ) can be calculated via the relation  $-Z' = R_s + R_{ct} + A_w \omega^{-0.5}$ , from the slope of the linear fitting between  $Z'$  and  $\omega^{-0.5}$  in the low

frequencies; Figure 5e, f. The  $D_{Mg}^{2+}$  values (Table 1) of  $S_1$  and  $S_2$  electrodes are around  $10^{-14} \text{ cm}^2 \text{s}^{-1}$  with HFE and become lower  $D_{Mg}^{2+} \sim 10^{-15} \text{ cm}^2 \text{s}^{-1}$  with PLI/HFE, indicative of slow electrochemical kinetics of the S cathode for Mg-ion storage; however, compared with typical Mg-storage materials like inorganic and organic cathodes ( $\text{Mo}_6\text{S}_8$ ,  $\text{TiS}_2$ ,  $\text{VS}_2$ ,  $\text{TiSe}_2$ ,  $\text{VSe}_2$ , and  $\text{PI@CNT}$  are  $10^{-12}$ ,  $10^{-22}$ ,  $10^{-22}$ ,  $10^{-19}$ ,  $10^{-19}$ , and  $10^{-12} \text{ cm}^2 \text{s}^{-1}$ , respectively),<sup>38</sup> the results reveal promising kinetics in the magnesiation/demagnesiation processes after further optimization. Figure S3a and b display the first discharge/charge curves of Mg/HFE/Sn and Mg/HFE/H\_Sn coin cells at the current density of  $20 \mu\text{A cm}^{-2}$  at room temperature and at  $55^\circ\text{C}$ , respectively. The Mg/HFE/ $S_1$  cell delivered the highest initial discharge capacity of  $\sim 2070 \text{ mAh g}^{-1}$  at  $55^\circ\text{C}$ . Mg/H\_Sn and Mg/ $S_1$  exhibit the activation process, followed by an extended discharge flat voltage plateau at  $\approx 1.25 \pm 0.1 \text{ V}$  versus  $\text{Mg/Mg}^{2+}$ . The observed prominent discharge voltage



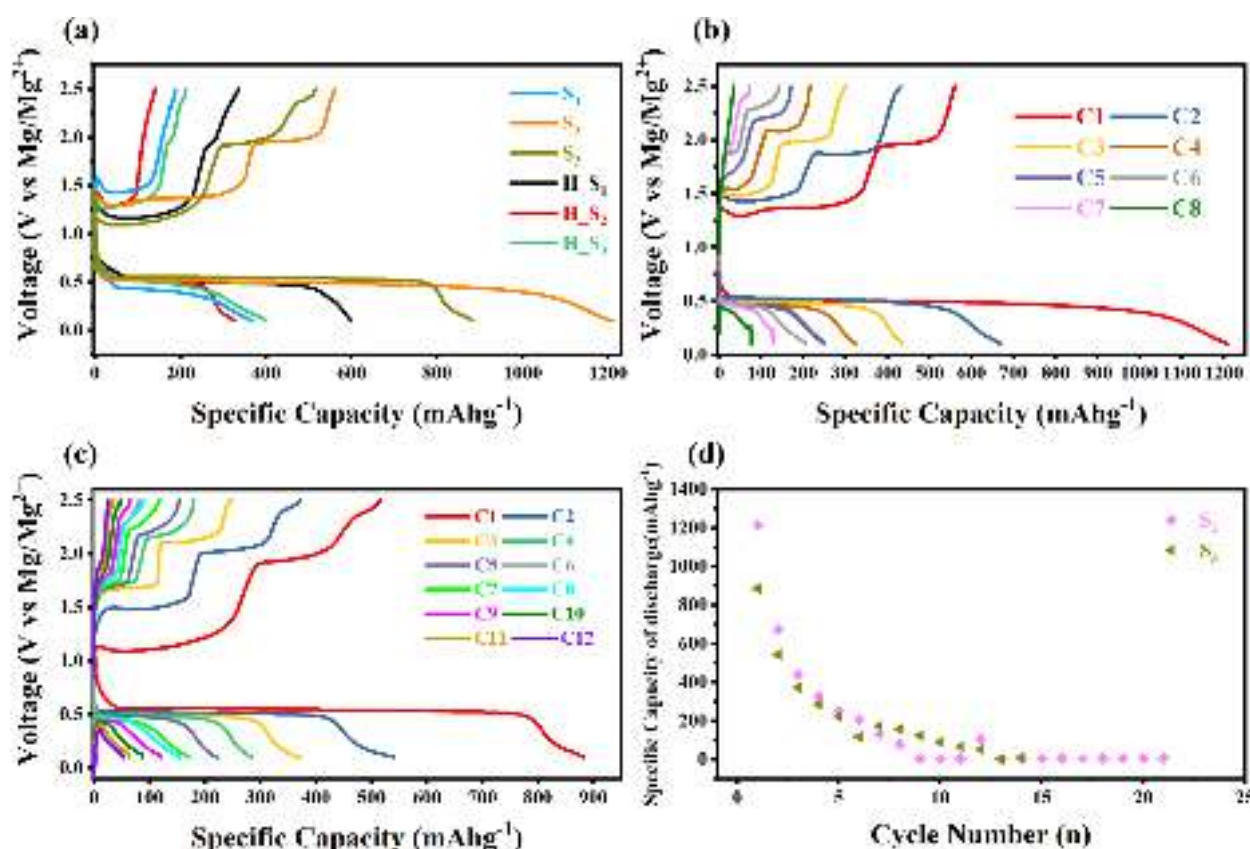


**Figure 6.** Galvanostatic discharge–charge curves of the samples for (a) PLI/HFE at 55 °C; (b) cycles of the sample [S<sub>2</sub>] for PLI/HFE; (c) cycles of the sample [S<sub>3</sub>] for PLI/HFE; and (d) specific capacity versus cycle number; at 55 °C.

increases, as shown in Figure S3b, can be attributed to the irreversible reactions between the Mg anode and the liquid electrolyte, especially with the increase in temperature. However, these phenomena disappeared after isolating the surface of the Mg from the liquid electrolyte by the PLI. Figure 6a displays the first discharge/charge curves of Mg/[PLI/HFE]/S<sub>n</sub> and Mg/[PLI/HFE]/H-S<sub>n</sub> coin cells at the current density of 20  $\mu\text{A cm}^{-2}$ . The Mg/[PLI/HFE]/S<sub>2</sub> cell delivered the highest initial discharge/charge capacity  $\sim 1210/560 \text{ mAh g}^{-1}$  at 55 °C with an extended discharge flat voltage plateau at  $\approx 0.6 \pm 0.1 \text{ V}$  versus Mg/Mg<sup>2+</sup>. Figure 6b, c displays the first 8 and 12 discharge/charge curves of Mg/[PLI/HFE]/S<sub>2</sub> and Mg/[PLI/HFE]/S<sub>3</sub> coin cells at 55 °C. The charge curves exhibit two obvious charge plateaus at  $\sim 1.2$  and  $1.8 \text{ V}$ , which are related to the successive Mg<sup>2+</sup> extraction from MgS<sub>x</sub> and MgS conversion phases, respectively.<sup>14</sup> The cycling performance of Mg/[PLI/HFE]/S<sub>1</sub> and Mg/[PLI/HFE]/H-S<sub>3</sub> coin cells are shown in Figure 6d. It is noteworthy that Mg/S<sub>n</sub> with the PLI/HFE electrolyte presents much better cycling performance than the HFE electrolyte. This fully proves that the PLI protective layer significantly enhances the interfacial compatibility of Mg metal by reducing the side reaction between the Mg metal and the HFE electrolyte.<sup>39</sup> To trace the evolution of the morphology, composition, and the structure of the sulfur cathode at different cycling states, Mg/[PLI/HFE]/S<sub>2</sub>, Mg/[HFE]/H-S<sub>1</sub>, and Mg/[HFE]/H-S<sub>3</sub> cells were discharged and discharged/charged at a constant capacity and disassembled to perform XRD, SEM, and EDS analyses. Figure 7a shows the XRD pattern of S<sub>2</sub> at different cycling states to study the impact of the initial magnesia/magnesia chemistry of Mg<sup>2+</sup> ions in the structure of S, the characteristic main peak (110) of S is left-

shifted to the lower  $2\theta$  values after the initial discharge, and its original position after recharge was restored, suggesting the reversible redox reaction of the sulfur species; Figure 7b. Furthermore, this negative shift can be related to the chemical coupling between S and Mg<sup>2+</sup> ions via conversion reaction accompanied by the contraction of the lattice. The equation  $\beta_{hkl} \cos \theta = \frac{K\lambda}{D} + 4\epsilon \sin \theta$  is the UDM (uniform deformation model) Williamson–Hall plots, where,  $\beta_{hkl}$ ,  $\theta$ ,  $K$ , and  $\lambda$  are the full width at half maximum (FWHM), Bragg's diffraction angle, the shape factor (0.89), and the wavelength of X-rays, respectively. From the graph of  $\beta \cos(\theta)$  as a function of  $4\sin(\theta)$ , as shown in Figure 7c, we can extract the size and strain from the y-intercept and the slope.

Table 2 lists the crystallite size and strain for sulfur powder and S<sub>2</sub> at different cycling states. The compressive micro-strain<sup>40</sup> was affected by the introduction of Mg<sup>2+</sup> ions in the framework of sulfur, and the value of  $\epsilon$  is decreased from 0.0017 for S<sub>2</sub> to 0.0006 after the initial discharge and increased to 0.0025 after recharge, suggesting the reversible compression and the contraction of S upon insertion and extraction of Mg<sup>2+</sup>. Figures 7d and S3c show the EDS spectra of H-S<sub>1</sub> and H-S<sub>3</sub> at different cycling states. The EDS results of H-S<sub>1</sub>/H-S<sub>3</sub> demonstrated that Mg wt. % increased from 0/0 for the pristine state to 5.86/9.61 wt. % after discharge, while the Mg wt. % decreased to 1.55/2.83 wt. % after recharge, which confirms a reversible conversion reaction procedure of Mg<sup>2+</sup> during a discharge/charge cycle, as mentioned before. Characteristic bands corresponding to F and Si were due to the PVDF used as a binder in electrode preparation and glass fiber as a separator, respectively. Figures 7e–g and S3d–f

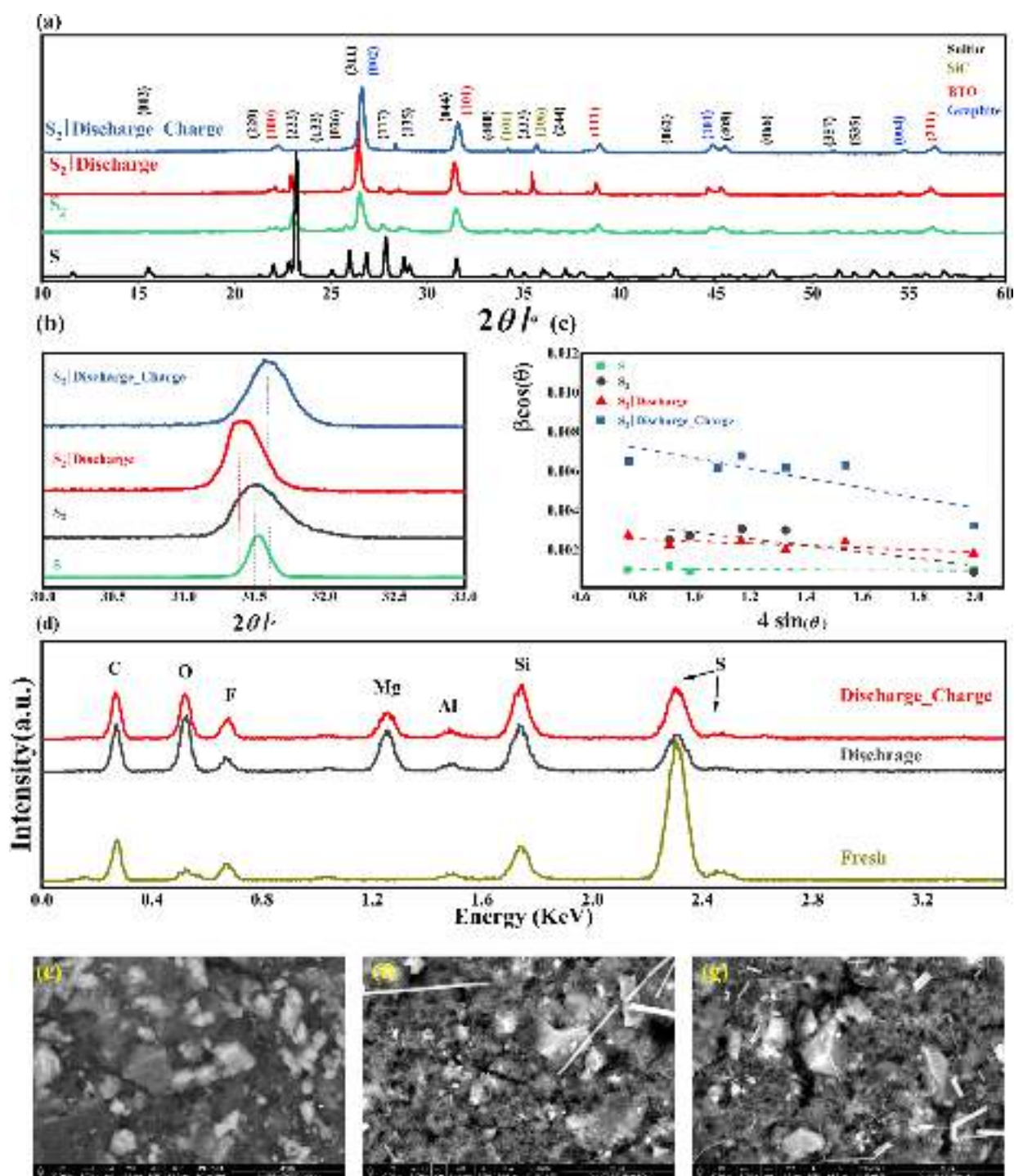


**Figure 7.** (a) XRD patterns of the sample [S<sub>2</sub>]; (b) zoomed image of XRD spectra in the range of 30–33°; (c) Williamson–Hall plots of sulfur; (d) EDS spectra; SEM micrographs of (e) fresh, (f) discharge, and (g) discharge–charge.

**Table 2. Crystallite Size and Strain for Sulfur Powder and S<sub>2</sub> at Different Cycling States**

samples	sulfur powder	S <sub>2</sub> /HFE/PLI pristine discharge–discharge– charge		
compressive macrostrain ( $\times 10^{-4}$ )	0.58	17	6	25.2
crystallite size D (nm)	131.65	31.48	48.27	15.74

present SEM images of H<sub>S</sub><sub>1</sub> and H<sub>S</sub><sub>3</sub> at the pristine state, discharged state, and discharged/charged state. Compared with the pristine electrode, crack formation, pores, and Mg needle precipitation were noticed at the first discharge of H<sub>S</sub><sub>1</sub> and H<sub>S</sub><sub>3</sub> electrodes. The degree of the crack formation, pores, and Mg needle precipitation grew and became more pronounced after the charging state of H<sub>S</sub><sub>1</sub> and H<sub>S</sub><sub>3</sub> electrodes.



## CONCLUSIONS

A simple HFE based on  $\text{Mg}(\text{NO}_3)_2$  dissolved in the cosolvent of ACN and G4 has been developed for realizing MgS batteries. A facile method was established to prepare a polymer interface as a protective layer mainly consisted of PVDF and  $\text{Mg}(\text{O}_3\text{SCF}_3)_2$ . Compared with liquid electrolytes, Mg symmetric cells using the interphase-protected Mg electrodes have demonstrated a low stable overpotential over 100 stable cycles at 55 °C because of improved electrode/electrolyte interfacial compatibility. Furthermore, a feasible strategy of anchoring polysulfides using  $\text{BaTiO}_3$  and SiC is proposed to achieve a stable S cathode for magnesium-ion batteries. The optimized  $\text{S}_2$  delivers higher reversible capacity (1200.8 mAh  $\text{g}^{-1}$ ) and a longer cycle life (12 cycles). HFE provides the promising potential to realize commercial MgS batteries. Future work with deep insight into the solvation structure, artificial interface, and impact of the high-donor-number solvents [e.g., dimethyl sulfoxide (DMSO)] may offer a promising strategy to optimize the current halogen-free electrolytes. Furthermore, to enhance the reaction kinetics of  $\text{Mg}^{2+}$ , ion doping and/or the nanostructure design of S cathodes for Mg-ion storage will be investigated in future studies.

## ASSOCIATED CONTENT

### Supporting Information

The Supporting Information is available free of charge at <https://pubs.acs.org/doi/10.1021/acsaem.1c03778>.

Comparison between the CE values at RT and 55 °C; CE calculation for the CVs at RT and at 55 °C; Nyquist plots of a Mg//PLI//Mg cell; galvanostatic discharge–charge curves; EDS and SEM micrographs of the  $\text{S}_3$  cathode at different cycling states (PDF)

## AUTHOR INFORMATION

### Corresponding Authors

Eslam Sheha – Physics Department, Faculty of Science, Benha University, 13518 Benha, Egypt; [orcid.org/0000-0002-8700-4906](https://orcid.org/0000-0002-8700-4906); Email: [islam.shihah@fsc.bu.edu.eg](mailto:islam.shihah@fsc.bu.edu.eg)

Niya Sa – Department of Chemistry, University of Massachusetts Boston, Boston, Massachusetts 02125, United States; Email: [niya.sa@umb.edu](mailto:niya.sa@umb.edu)

### Authors

Mohamed Farrag – Physics Department, Faculty of Science, Benha University, 13518 Benha, Egypt

Shengqi Fan – Department of Chemistry, University of Massachusetts Boston, Boston, Massachusetts 02125, United States

Eman Kamar – Chemistry Department, Faculty of Science, Benha University, 13518 Benha, Egypt

Complete contact information is available at: <https://pubs.acs.org/doi/10.1021/acsaem.1c03778>

### Notes

The authors declare no competing financial interest.

## ACKNOWLEDGMENTS

This work is financially supported by the Academy of Scientific Research Technology/Bibliotheca Alexandrina (ASRT/BA) (Grant No. 1530) and Science Technology Development Fund (Grant No. 30340). N.S. would like to thank the financial

support from National Science Foundation (NSF) MRI for the acquisition of the advanced FESEM (grant no. 1919919) and the NSF CAREER Award (grant no. 2047753). This work is also financially supported by the Start-up Funds of the University of Massachusetts Boston.

## REFERENCES

- (1) Wu, D.; Ren, W.; Yang, Y.; Wang, J.; NuLi, Y. A Se-Doped S@CMK3 Composite as a High-Performance Cathode for Magnesium–Sulfur Batteries with  $\text{Mg}^{2+}/\text{Li}^+$  Hybrid Electrolytes. *J. Phys. Chem. C* **2021**, *125*, 25959–25967.
- (2) Zhao, Q.; Wang, R.; Zhang, Y.; Huang, G.; Jiang, B.; Xu, C.; Pan, F. The design of  $\text{CoS}_4\text{@MXene}$  heterostructure as sulfur host to promote the electrochemical kinetics for reversible magnesium–sulfur batteries. *J. Magnesium Alloys* **2021**, *9*, 78–89.
- (3) Gao, T.; Hou, S.; Wang, F.; Ma, Z.; Li, X.; Xu, K.; Wang, C. Reversible  $\text{S}_0/\text{MgS}_x$  Redox Chemistry in a  $\text{MgTFSI}_2/\text{MgCl}_2/\text{DME}$  Electrolyte for Rechargeable Mg/S Batteries. *Angew. Chem., Int. Ed.* **2017**, *56*, 13526–13530.
- (4) Bi, Y.; He, S.; Fan, C.; Luo, J.; Yuan, B.; Liu, T. L. A robust ionic liquid magnesium electrolyte enabling Mg/S batteries. *J. Mater. Chem. A* **2020**, *8*, 12301–12305.
- (5) Sun, J.; Deng, C.; Bi, Y.; Wu, K.-H.; Zhu, S.; Xie, Z.; Li, C.; Amal, R.; Luo, J.; Liu, T.; Wang, D.-W. In Situ Sulfurized Carbon-Confined Cobalt for Long-Life Mg/S Batteries. *ACS Appl. Energy Mater.* **2020**, *3*, 2516–2525.
- (6) Gao, T.; Ji, X.; Hou, S.; Fan, X.; Li, X.; Yang, C.; Han, F.; Wang, F.; Jiang, J.; Xu, K. Thermodynamics and kinetics of sulfur cathode during discharge in  $\text{MgTFSI}_2$ –DME electrolyte. *Adv. Mater.* **2018**, *30*, No. 1704313.
- (7) Bieker, G.; Küpers, V.; Kolek, M.; Winter, M. Intrinsic differences and realistic perspectives of lithium–sulfur and magnesium–sulfur batteries. *Commun. Mater.* **2021**, *2*, 1–12.
- (8) Yang, Y.; Wang, W.; Nuli, Y.; Yang, J.; Wang, J. High active magnesium trifluoromethanesulfonate-based electrolytes for magnesium–sulfur batteries. *ACS Appl. Mater. Interfaces* **2019**, *11*, 9062–9072.
- (9) He, S.; Nielson, K. V.; Luo, J.; Liu, T. L. Recent advances on  $\text{MgCl}_2$  based electrolytes for rechargeable Mg batteries. *Energy Storage Mater.* **2017**, *8*, 184–188.
- (10) Huang, D.; Tan, S.; Li, M.; Wang, D.; Han, C.; An, Q.; Mai, L. Highly efficient non-nucleophilic  $\text{Mg}(\text{CF}_3\text{SO}_3)_2$ -based electrolyte for high-power Mg/S battery. *ACS Appl. Mater. Interfaces* **2020**, *12*, 17474–17480.
- (11) Luo, J.; He, S.; Liu, T. L. Tertiary  $\text{Mg}/\text{MgCl}_2/\text{AlCl}_3$  Inorganic  $\text{Mg}^{2+}$  Electrolytes with Unprecedented Electrochemical Performance for Reversible Mg Deposition. *ACS Energy Lett.* **2017**, *2*, 1197–1202.
- (12) Du, A.; Zhang, Z.; Qu, H.; Cui, Z.; Qiao, L.; Wang, L.; Chai, J.; Lu, T.; Dong, S.; Dong, T. An efficient organic magnesium borate-based electrolyte with non-nucleophilic characteristics for magnesium–sulfur battery. *Energy Environ. Sci.* **2017**, *10*, 2616–2625.
- (13) Luo, J.; Bi, Y.; Zhang, L.; Zhang, X.; Liu, T. L. A Stable, Non-Corrosive Perfluorinated Pinacolatoborate Mg Electrolyte for Rechargeable Mg Batteries. *Am. Chem. Soc. Div. Polym. Chem.* **2019**, *131*, 7041–7045.
- (14) Zhao-Karger, Z.; Liu, R.; Dai, W.; Li, Z.; Diemant, T.; Vinayan, B.; Bonatto Minella, C.; Yu, X.; Manthiram, A.; Behm, R. J. R. Toward highly reversible magnesium–sulfur batteries with efficient and practical  $\text{Mg}[\text{B}(\text{hfp})_4]_2$  electrolyte. *ACS Energy Lett.* **2018**, *3*, 2005–2013.
- (15) Ji, Y.; Liu-Théato, X.; Xiu, Y.; Indris, S.; Njel, C.; Maibach, J.; Ehrenberg, H.; Fichtner, M.; Zhao-Karger, Z. Polyoxometalate Modified Separator for Performance Enhancement of Magnesium–Sulfur Batteries. *Adv. Funct. Mater.* **2021**, *31*, No. 2100868.
- (16) Li, Y.; Guan, S.; Huo, H.; Ma, Y.; Gao, Y.; Zuo, P.; Yin, G. A Review of Magnesium Aluminum Chloride Complex Electrolytes for Mg Batteries. *Adv. Funct. Mater.* **2021**, *31*, No. 2100650.
- (17) Ford, H. O.; Doyle, E. S.; He, P.; Boggess, W. C.; Oliver, A. G.; Wu, T.; Sterbinsky, G. E.; Schaefer, J. L. Self-discharge of

magnesium–sulfur batteries leads to active material loss and poor shelf life. *Energy Environ. Sci.* **2021**, *14*, 890–899.

(18) Hou, S.; Ji, X.; Gaskell, K.; Wang, P.-F.; Wang, L.; Xu, J.; Sun, R.; Borodin, O.; Wang, C. Solvation sheath reorganization enables divalent metal batteries with fast interfacial charge transfer kinetics. *Science* **2021**, *374*, 172–178.

(19) Zhou, X.; Tian, J.; Hu, J.; Li, C. High rate magnesium–sulfur battery with improved cyclability based on metal–organic framework derivative carbon host. *Adv. Mater.* **2018**, *30*, No. 1704166.

(20) Wang, W.; Wu, L.; Li, Z.; Ma, S.; Dou, H.; Zhang, X. Rational Design of a Piezoelectric BaTiO<sub>3</sub> Nanodot Surface-Modified LiNi<sub>0.6</sub>Co<sub>0.2</sub>Mn<sub>0.2</sub>O<sub>2</sub> Cathode Material for High-Rate Lithium-Ion Batteries. *ChemElectroChem* **2020**, *7*, 3646–3652.

(21) Zhao, Z.; Li, G.; Wang, Z.; Feng, M.; Sun, M.; Xue, X.; Liu, R.; Jia, H.; Wang, Z.; Zhang, W. Black BaTiO<sub>3</sub> as multifunctional sulfur immobilizer for superior lithium sulfur batteries. *J. Power Sources* **2019**, *434*, No. 226729.

(22) Xie, K.; You, Y.; Yuan, K.; Lu, W.; Zhang, K.; Xu, F.; Ye, M.; Ke, S.; Shen, C.; Zeng, X. Ferroelectric-enhanced polysulfide trapping for lithium–sulfur battery improvement. *Adv. Mater.* **2017**, *29*, No. 1604724.

(23) Son, B. D.; Cho, S. H.; Bae, K. Y.; Kim, B. H.; Yoon, W. Y. Dual functional effect of the ferroelectricity embedded interlayer in lithium sulfur battery. *J. Power Sources* **2019**, *419*, 35–41.

(24) Zhao, Y.; Zhao, J.; Cai, Q. SiC<sub>2</sub> siligraphene as a promising anchoring material for lithium-sulfur batteries: a computational study. *Appl. Surf. Sci.* **2018**, *440*, 889–896.

(25) Song, N.; Gao, Z.; Zhang, Y.; Li, X. B4C nanoskeleton enabled, flexible lithium-sulfur batteries. *Nano Energy* **2019**, *58*, 30–39.

(26) Wang, J.; Wang, W.; Li, H.; Tan, T.; Wang, X.; Zhao, Y. Carbon nanotubes/SiC prepared by catalytic chemical vapor deposition as scaffold for improved lithium-sulfur batteries. *J. Nanopart. Res.* **2019**, *21*, 1–10.

(27) Sheha, E., Magnesium Battery. In *Electrochemical Devices for Energy Storage Applications*, 1st ed.; Kebede, M. A.; Ezema, F.I., Ed. CRC Press, 2020.

(28) Yang, L.; Yang, C.; Chen, Y.; Pu, Z.; Zhang, Z.; Jie, Y.; Zheng, X.; Xiao, Y.; Jiao, S.; Li, Q. Hybrid MgCl<sub>2</sub>/AlCl<sub>3</sub>/Mg (TFSI)<sub>2</sub> Electrolytes in DME Enabling High-Rate Rechargeable Mg Batteries. *ACS Appl. Mater. Interfaces* **2021**, *13*, 30712–30721.

(29) Shen, Y.; Zhang, Q.; Wang, Y.; Gu, L.; Zhao, X.; Shen, X. A Pyrite Iron Disulfide Cathode with a Copper Current Collector for High-Energy Reversible Magnesium-Ion Storage. *Adv. Mater.* **2021**, *33*, No. 2103881.

(30) Horia, R.; Nguyen, D.-T.; Eng, A. Y. S.; Seh, Z. W. Using a chloride-free magnesium battery electrolyte to form a robust anode–electrolyte nanointerface. *Nano Lett.* **2021**, *21*, 8220–8228.

(31) Ahn, W.; Kim, K.-B.; Jung, K.-N.; Shin, K.-H.; Jin, C.-S. Synthesis and electrochemical properties of a sulfur-multi walled carbon nanotubes composite as a cathode material for lithium sulfur batteries. *J. Power Sources* **2012**, *202*, 394–399.

(32) Zhou, W.; Liu, J.; Chen, T.; Tan, K. S.; Jia, X.; Luo, Z.; Cong, C.; Yang, H.; Li, C. M.; Yu, T. Fabrication of Co<sub>3</sub>O<sub>4</sub>-reduced graphene oxide scrolls for high-performance supercapacitor electrodes. *Phys. Chem. Chem. Phys.* **2011**, *13*, 14462–14465.

(33) Dong, X.-C.; Xu, H.; Wang, X.-W.; Huang, Y.-X.; Chan-Park, M. B.; Zhang, H.; Wang, L.-H.; Huang, W.; Chen, P. 3D graphene–cobalt oxide electrode for high-performance supercapacitor and enzymeless glucose detection. *ACS Nano* **2012**, *6*, 3206–3213.

(34) Muralidhar, C.; Pillai, P. XRD studies on barium titanate (BaTiO<sub>3</sub>)/polyvinylidene fluoride (PVDF) composites. *J. Mater. Sci.* **1988**, *23*, 410–414.

(35) Wang, H.-E.; Yin, K.; Zhao, X.; Qin, N.; Li, Y.; Deng, Z.; Zheng, L.; Su, B.-L.; Lu, Z. Coherent TiO<sub>2</sub>/BaTiO<sub>3</sub> heterostructure as a functional reservoir and promoter for polysulfide intermediates. *Chem. Commun.* **2018**, *54*, 12250–12253.

(36) Zhang, R.; Cui, C.; Li, R.; Li, Y.; Du, C.; Gao, Y.; Huo, H.; Ma, Y.; Zuo, P.; Yin, G. An Artificial Interphase Enables the Use of Mg

(TFSI) 2-Based Electrolytes in Magnesium Metal Batteries. *Chem. Eng. J.* **2021**, *426*, No. 130751.

(37) Sheha, E.; Refai, H. Water scavenger as effective electrolyte additive and hybrid binder-free organic/inorganic cathode for Mg battery applications. *Electrochim. Acta* **2021**, *372*, No. 137883.

(38) Xiu, Y.; Li, Z.; Bhaghavathi Parambath, V.; Ding, Z.; Wang, L.; Reupert, A.; Fichtner, M.; Zhao-Karger, Z. Combining Quinone-Based Cathode with an Efficient Borate Electrolyte for High-Performance Magnesium Batteries. *Batteries Supercaps* **2021**, 1850.

(39) Zhao, Y.; Du, A.; Dong, S.; Jiang, F.; Guo, Z.; Ge, X.; Qu, X.; Zhou, X.; Cui, G. A Bismuth-Based Protective Layer for Magnesium Metal Anode in Noncorrosive Electrolytes. *ACS Energy Lett.* **2021**, *6*, 2594–2601.

(40) Ghosh, M. P.; Datta, S.; Sharma, R.; Tanbir, K.; Kar, M.; Mukherjee, S. Copper doped nickel ferrite nanoparticles: Jahn-Teller distortion and its effect on microstructural, magnetic and electronic properties. *Mater. Sci. Eng., B* **2021**, *263*, No. 114864.